Tectonophysics 816 (2021) 229014

Contents lists available at ScienceDirect

Tectonophysics

journal homepage: www.elsevier.com/locate/tecto

Crustal azimuthal anisotropy and deformation beneath the northeastern Tibetan Plateau and adjacent areas: Insights from receiver function analysis

Tuo Zheng [a,b,*], Stephen S. Gao [b], Zhifeng Ding [c], Kelly H. Liu [b], Lijun Chang [c], Xiaoping Fan [a], Fansheng Kong [d], Youqiang Yu [e]

[a] College of Transportation Science and Engineering, Nanjing Tech University, Nanjing 210009, China
[b] Geology and Geophysics Program, Missouri University of Science and Technology, Rolla, MO 65409, USA
[c] Institute of Geophysics, China Earthquake Administration, Beijing 100081, China
[d] Second Institute of Oceanography, State Oceanic Administration & Second Institute of Oceanography, Ministry of Natural Resources, Hangzhou 310012, China
[e] State Key Laboratory of Marine Geology, Tongji University, Shanghai 200092, China

ARTICLE INFO

Keywords:
Northeastern Tibetan Plateau
Receiver function
Seismic anisotropy
Crustal deformation

ABSTRACT

We present crustal azimuthal anisotropy measurements at 246 stations by fitting the sinusoidal moveout of P-to-S receiver functions to infer crustal deformation field in the northeastern (NE) Tibetan Plateau and adjacent areas. The dominant orientation of the observed crustal anisotropy shows a systematic spatial variation: NW-SE in the NE Tibetan Plateau and western Alxa Block, nearly NE-SW in the eastern Alxa Block and Yinchuan-Hetao Graben, and E-W in the eastern portion of the Western Qinling Terrane. The magnitude of crustal anisotropy varies from 0.15 to 0.75 s with an average of 0.36 ± 0.11 s. Fault parallel crustal anisotropy with large magnitudes observed in the NE Tibetan Plateau provides independent constraints on the lateral extent of the deformation zone associated with the faults. The observed spatial distribution of crustal anisotropy, when combined with previous crustal velocity and Poisson's ratio measurements, implies that channel flow in the middle-to-lower crust is unlikely to exist beneath the NE Tibetan Plateau. The main characteristics of crustal anisotropy observed in the western Alxa Block are similar to areas affected by the Indo-Eurasian collision, while those observed in the eastern Alxa Block are comparable to the stable North China Craton.

1. Introduction

The study area (Fig. 1) is a tectonically diverse region where the Tibetan Plateau, North China Craton and Yangtze Craton interact with each other, and thus is an ideal natural laboratory for understanding continental crustal deformation associated with interactions among tectonic blocks. While it is commonly believed that major active faults and strong earthquakes in the area are mostly due to the collision between the Indian and Eurasian plates (Yin and Harrison, 2000), mechanisms responsible for the uplift and lateral growth of the Tibetan Plateau remain enigmatic. Several geodynamic models, including (1) continuous shortening of both crust and lithospheric mantle (e.g., Molnar and Tapponnier, 1975; England and Houseman, 1986), (2) discrete intracontinental subduction coupled with strike-slip extrusion (e.g., Tapponnier et al., 2001), and (3) lateral channel flow in the middle-to-lower crust (e.g., Clark and Royden, 2000), have been proposed.

One of the geophysical constraints that can be used to characterize the geodynamic model responsible for the uplifting and expansion of the Tibetan Plateau is seismic azimuthal anisotropy, which can be quantified by measuring the dependence of propagation velocity on polarization orientation of the shear wave. In the lithosphere, azimuthal anisotropy is generally believed to be closely associated with the stress and/or strain field at depth, and thus can offer important insights into the lithospheric deformation characteristics (e.g., Silver, 1996). Laboratory and field studies suggest that azimuthal anisotropy in the upper crust is mostly produced by the preferred orientation of fluid-saturated microcracks (e.g., Crampin, 1978; Rasolofosaon et al., 2000), and anisotropy in the lower crust and upper mantle, due to the closure of the cracks, is usually attributed to strain-induced lattice preferred orientation of intrinsically anisotropic minerals, principally mica, amphibole, and olivine (Zhang and Karato, 1995; Tatham et al., 2008).

Numerous seismic anisotropy studies have been conducted in the vicinity of the northeastern (NE) Tibetan Plateau. XKS (including the

* Corresponding author at: College of Transportation Science and Engineering, Nanjing Tech University, Nanjing 210009, China.
E-mail address: zhengtu@mst.edu (T. Zheng).

https://doi.org/10.1016/j.tecto.2021.229014
Received 13 January 2021; Received in revised form 26 July 2021; Accepted 2 August 2021
Available online 9 August 2021

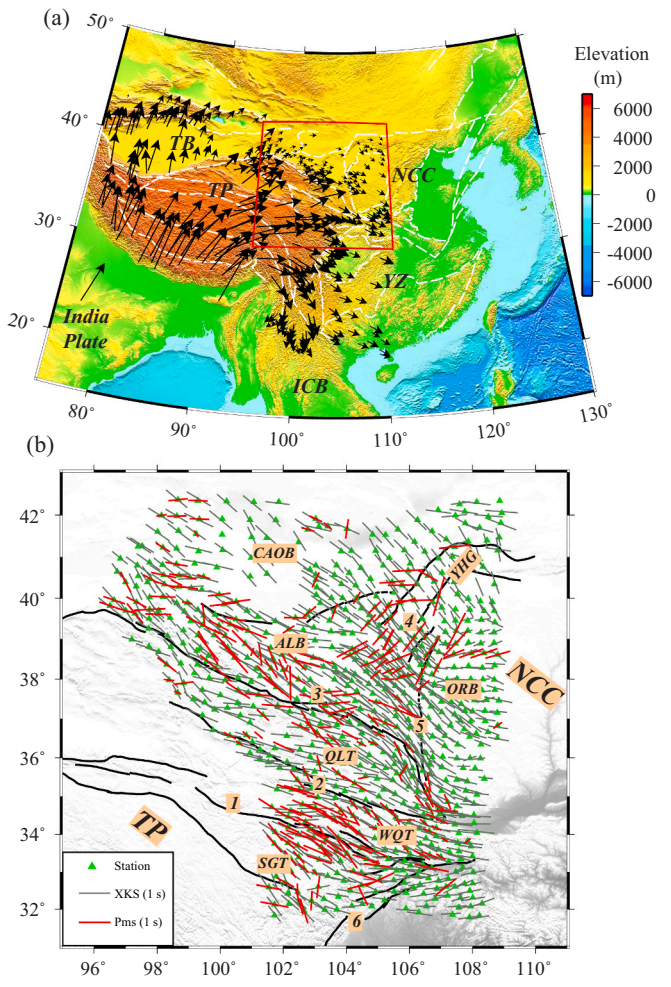

Fig. 1. (a) A topographic relief map of China and adjacent areas, showing GPS velocities relative to the stable Eurasian Plate (black arrows; Gan et al., 2007). The white lines represent sutures and boundaries of major tectonic blocks. The red box marks the study area. ICB: Indo-China Block; NCC: North China Craton; TB: Tarim Block; TP: Tibetan Plateau; YZ: Yangtze Craton. (b) Major tectonic units in the study area showing seismic stations used in this study (triangles). The red bars denote previous crustal anisotropy observations (Shen et al., 2015; Wang et al., 2016; Xu et al., 2018), and the gray bars indicate previous XKS splitting measurements (Chang et al., 2017). The orientation of the bars indicates the fast orientation of anisotropy, and the length is proportional to the strength of anisotropy. Black lines represent major active faults. 1: East Kunlun Fault; 2: Qinling Fault; 3: Qilian-Haiyuan Fault; 4: Helanshan Fault; 5: Qingtongxia-Guyuan Fault; 6: Longmenshan Fault. ALB: Alxa Block; CAOB: Central Asia Orogenic Belt; ORB: Ordos Block; QLT: Qilian Terrane; SGT: Songpan-Ganzi Terrane; WQT: Western Qinling Terrane; YHG: Yinchuan-Hetao Graben. (For interpretation of the references to colour in this figure legend, the reader is referred to the web version of this article.)

SKS, SKKS, and PKS phases) splitting analyses (Ye et al., 2016; Chang et al., 2017; Huang et al., 2017; Gao et al., 2019; Zhu and Ma, 2021), which measure azimuthal anisotropy from the core mantle boundary to the surface on the receiver side, suggest significant lateral variations of seismic anisotropy across NE Tibet. Surface wave anisotropic tomography studies (Xie et al., 2013, 2017; Hacker et al., 2014) show NW-SE fast orientations for both the crust and the upper mantle beneath the NE Tibetan Plateau, indicating a coupled deformation throughout the whole lithosphere. A P-wave anisotropic tomography study (Huang et al., 2014) finds NE-SW fast orientations at 25 and 40 km depths and supports the existence of channel flow in the middle-to-lower crust beneath the NE Tibetan Plateau.

Several studies (Fig. 1b) have utilized source-normalized P-to-S conversions (receiver functions or RFs) from the Moho to reveal seismic azimuthal anisotropy in the entire crust beneath the NE Tibetan Plateau and adjacent areas (Shen et al., 2015; Wang et al., 2016; Xu et al., 2018), with various spatial coverages and different conclusions regarding the characteristics of crustal deformation. Shen et al. (2015) analyze crustal anisotropy at 19 permanent stations and argue that the observed crustal anisotropy is consistent with the existence of lower crustal flow beneath the NE Tibetan Plateau. In contrast, Wang et al. (2016) utilize a joint analysis of P_ms phases from RFs (Liu and Niu, 2012) to extract crustal anisotropy measurements at 12 out of 171 permanent stations. They suggest that coherent shortening of the entire lithosphere is likely the main mechanism of lithospheric deformation, which is inconsistent with the conclusion from Shen et al. (2015). Similarly, Xu et al. (2018) apply the joint analysis technique (Liu and Niu, 2012) to the dense seismic array to obtain 221 crustal anisotropy measurements, and the significant discrepancies between the resulting fast orientations and proposed flow direction (Clark and Royden, 2000) are inconsistent with the presence of lower crustal flow.

Similar to the NE Tibetan Plateau, considerable controversies regarding crustal structure and deformation exist in the neighboring blocks of the plateau. For instance, while earlier studies generally consider the Alxa Block and Ordos Block to be integrated components of the North China Craton (e.g., Shen et al., 2017), some recent studies (e.g., Yu and Chen, 2016; Wang et al., 2017b) suggest that the two blocks may have been significantly modified by the extrusion of the NE Tibetan Plateau. Additionally, Zhang et al. (2018) interpret the observed anomalously high S velocity zone beneath the Alxa Block as a thick and rigid craton root, whereas a teleseismic P-wave tomography study (Guo et al., 2017) suggests that the low velocity anomalies beneath the Alxa Block are closely related to those beneath the Tibetan Plateau and thus might represent the northward extension of the plateau.

A refined characterization of lithospheric deformation beneath the NE Tibetan Plateau and adjacent areas, including the Alxa Block to the north, the Yinchuan-Hetao Graben to the northeast, and the Ordos Block to the east, can provide important information for elucidating the uplift and lateral growth of the Tibetan Plateau and geological evolution of the North China Craton. However, due to the influence of the sediments (Wang et al., 2017b) on the RFs, crustal anisotropy measurements are not available at many stations in the Ordos Block, Yinchuan-Hetao Graben, and Alxa Block (Fig. 1b; Shen et al., 2015; Wang et al., 2016; Xu et al., 2018). The limited spatial coverage of crustal anisotropy prevents in-depth investigation of lithospheric deformation mechanisms beneath the NE Tibetan Plateau and adjacent areas. The current study utilizes a recently developed frequency domain deconvolution procedure (Yu et al., 2015) to remove the strong reverberations on the RFs associated with a low-velocity layer, and measures crustal anisotropy at stations in a large scale dense portable array covering the NE Tibetan Plateau and adjacent regions. As detailed below, the greatly increased station coverage over previous studies plays a key role in delineating previously unrecognized features of crustal anisotropy and in constraining the formation mechanisms of the observed crustal anisotropy.

2. Data and methods

2.1. Data

The three component seismic data used in the study were recorded by 673 broadband stations in the NE Tibetan Plateau and adjacent areas (Fig. 1b), recorded between September 2013 and April 2016. The stations were part of the second phase deployment of the ChinArray project (ChinArray-Himalaya II). Each station was equipped with a Guralp CMG-3ESP or CMG-3ESPC sensor (60 s–50 Hz) and a Reftek-130 data logger. The stations had an average interstation distance of approximately 35 km which is approximately half of that of the USArray project.

The original RFs used in this study were extracted by Wang et al. (2017b), after component orientation checking and necessary

correction. A total of 569 teleseismic events with a magnitude M_W greater than 5.0 and epicentral distances between 30° and 90° were selected for the calculation of RFs. Fig. 2 shows the locations of these seismic events, which have a decent back-azimuthal (BAZ) coverage. The selected time window for computing the RFs is from 10 s before to 150 s after the first P arrival. All the waveform records were band-pass filtered with corner frequencies of 0.02 and 1 Hz. To calculate the RFs, the two horizontal (N-S and E-W) components were rotated into the radial (R) and transverse (T) components, and were then deconvolved by the vertical component (Z) by applying the time-domain iterative deconvolution procedure (Ligorria and Ammon, 1999).

We used a signal-to-noise ratio based technique (Gao and Liu, 2014) to ensure the quality of the RFs, and then we visually inspected the selected RFs and removed those without a clear first P arrival. After the RF selection procedure, a total of 81, 685 radial and transverse RF pairs were retained at 673 stations, and the number of RF pairs per station ranges from 12 to 210, with an average of 122. A comparison of the radial and transverse RFs, especially those recorded by stations situated on the bedrock where the P_ms phase is usually more unambiguously observed than those sitting on loose sediment, demonstrates that the signal-to-noise ratio of the P_ms on the transverse RFs (Fig. 3c) is much lower than that on the radial RFs (Fig. 3a). Consequently, while some of the studies also use transverse RFs to conduct crustal anisotropy measurements (e.g., Rumpker et al., 2014; Shen et al., 2015; Wang et al., 2016), the portable seismic array has a shorter observation period than permanent seismic network and thus has a limited number of available events, especially in the NE Tibetan Plateau where the crust is thick, highly attenuative, and structurally complex, resulting in a relatively low signal-to-noise ratio on the transverse RFs. Therefore, in this study only the radial RFs were used to investigate crustal anisotropy.

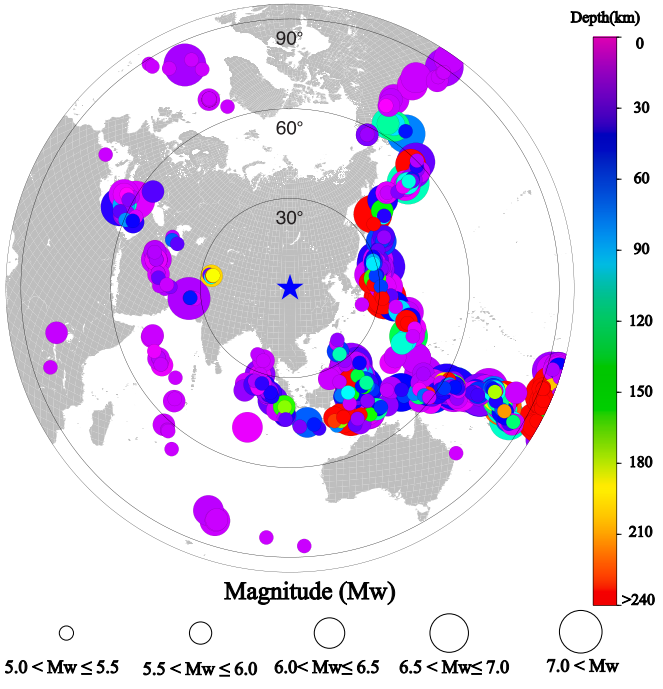

Fig. 2. Locations of teleseismic events (circles) used in this study. For a given event, the size of the circles is proportional to the magnitude (Mw), and the color of the circle corresponds to the focal depth. The circles labeled as 30°, 60°, and 90° denote epicentral distances from the center of study area (37°N, 104°E, marked as a blue star). (For interpretation of the references to colour in this figure legend, the reader is referred to the web version of this article.)

2.2. Effects of a low velocity sedimentary layer

Recent studies (Wang et al., 2017a, 2017b) have identified and characterized a thick sedimentary layer beneath the Yinchuan-Hetao Graben, Ordos Block, and western Alxa Block. The Yinchuan-Hetao Graben has a maximum sedimentary thickness of approximately 10 km, and the sedimentary thickness of the Ordos Block varies from 3 to 6 km, with an average thickness of 4 km (Wang et al., 2017b). The top part of the sedimentary layer possesses low seismic velocities and may cause a delayed largest peak on the radial RFs and strong reverberations (Zelt and Ellis, 1999; Yu et al., 2015).

Fig. 3 shows RFs from a station situated on the bedrock and those from a station located in a sedimentary basin. The largest arrival of the radial RFs of the basin station (Fig. 3b) is P_bs, which is the P-to-S conversion from the bottom of the low velocity sedimentary layer (Zelt and Ellis, 1999). The strong reverberations generated from the low velocity sedimentary layer can mask the P-to-S conversions associated with the Moho discontinuity (Yu et al., 2015; Zheng et al., 2019), making it difficult to reliably apply most receiver function methods to study crustal structure and anisotropy. In particular, Liu et al. (2017b) found that the deep basin in the Upper Mississippi Embayment can produce an error of up to 10 km in the resulting crustal thickness if the effect of decaying periodic arrivals of the reverberations on the RFs is not properly removed. Additionally, Zheng et al. (2019) suggest that the sedimentary effects on the RFs could lead to erroneous measurements of crustal anisotropy in the North China Craton (more than 40° in the fast orientation and 0.35 s in the magnitude of the resulting anisotropy). In this study, we apply a frequency domain resonance-removal filter (Yu et al., 2015) to eliminate or significantly reduce the influence of the strong reverberations associated with the low velocity layer.

2.3. Estimate of crustal anisotropy

The main goal of this study is to investigate the bulk crustal azimuthal anisotropy under the assumption of a horizontal axis of symmetry and flat Moho discontinuity (e.g., Nagaya et al., 2008; Liu and Niu, 2012). Detailed description of the applied technique can be found in Rumpker et al. (2014) and Kong et al. (2016). For a simple anisotropic layer with a horizontal symmetric axis, the arrival times of the P_ms phases can be expressed as a cosine function of the BAZ (Liu and Niu, 2012; Rumpker et al., 2014), i.e.,

$$t = t_0 - \frac{\delta t}{2} cos[2(\varphi - \theta)] \quad (1)$$

where t_0 represents the arrival time of the P_ms phase in the isotropic model; φ denotes the fast orientation (measured clockwise from the north) along which the P_ms phase has the earliest arrival; δt is the magnitude of crustal anisotropy; and θ represents the BAZ of the events. The two anisotropic parameters (φ and δt) quantify the orientation and strength of crustal anisotropy, respectively, and can be measured as follows: t_0 is set as 4.0 to 9.0 s with a step of 0.1 s, and the corresponding amplitudes are stacked according to Eq. (1), for fixed values of anisotropy parameters. The stacking is repeated using another combination of anisotropy parameters (0 to 1.0 s with a time interval of 0.05 s for δt, and − 90 to 90° with an increment of 1° for φ). Note that this study only searches for the stacked amplitude before and after 0.5 s each assumed t_0. The procedure is repeated for the next value of t_0, until we obtain a maximum stacked amplitude.

The following steps were then utilized in order to obtain reliable crustal anisotropy measurements (Kong et al., 2016): (1) performing moveout correction to correct the moveout of RFs as a function of the ray parameter to a reference epicentral distance of 60°; (2) stacking RFs in 10° BAZ bins to enhance the signal-to-noise ratio; (3) removing stations if the number of BAZ bands is less than 12 out of the 36 possible bands, or if there is a gap of 180° or greater in BAZ coverage; (4) manually

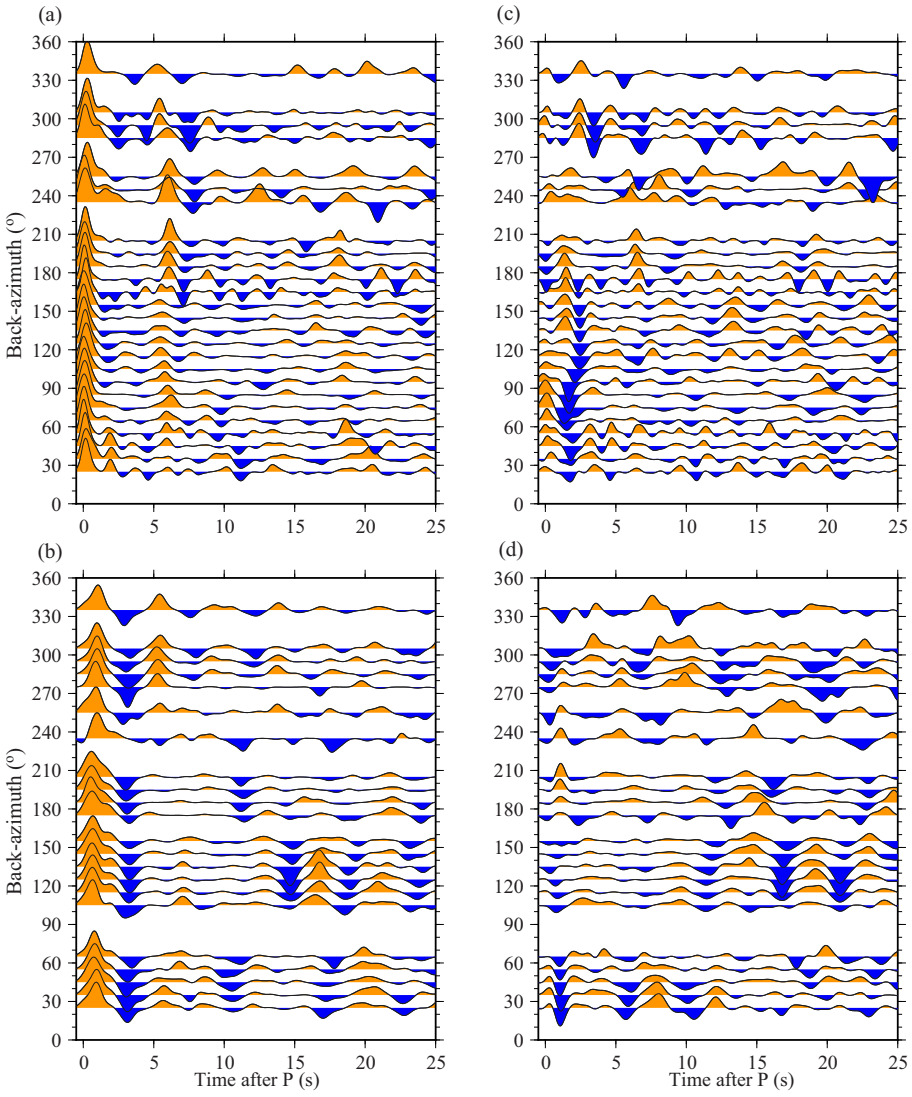

Fig. 3. Example receiver functions plotted as a function of the back-azimuths. (a) Radial RFs recorded by Station 62337 (34.5°N, 104.2°E) situated on bedrock. Positive amplitudes are shaded in orange, and negative in blue. (b) Radial RFs recorded by Station 15627 (39.2°N, 105.3°E) located in a sedimentary basin. Note that in (b), the delayed largest peak is the P-to-S conversion from the base of a low velocity sedimentary layer. (c) Transverse RFs of Station 62337. (d) Transverse RFs of Station 15627. (For interpretation of the references to colour in this figure legend, the reader is referred to the web version of this article.)

checking the RFs, and selecting only stations demonstrating clear, smooth, and coherent azimuthal variation of the P_ms phases, and removing stations with significant bifurcations and sharp offsets of the P_ms phases; (5) employing a bootstrap resampling technique (Efron and Tibshirani, 1986; Liu et al., 2003) to evaluate the uncertainties of crustal anisotropy measurements. In order for the resulting anisotropy parameters to be kept, the resulting combined standard deviations after 10 iterations for the measurements of a given station should be less than 0.4 in the analysis according to the following equation:

$$\sigma = \frac{\sigma_{\delta t}}{1.0} + \frac{\sigma_{\varphi}}{90.0} \tag{2}$$

where $\sigma_{\delta t}$ is the linear standard deviation for δt, and σ_{φ} is the circular standard deviation of φ. Eq. (2) is used for normalizing the misfits of the resulting anisotropy parameters, which have a maximum uncertainty of 90° for φ and about 1.0 s for δt. This study selects a σ value of 0.4 as the threshold (Kong et al., 2016; Zheng et al., 2018, 2019) because a station with a σ greater than this value may have an equivalent σ_{φ} greater than 35° or a $\sigma_{\delta t}$ greater than 0.4 s, which indicate significant uncertainty of the results. In addition, $\sigma_{\delta t}$ cannot be greater than the corresponding δt value. Figs. S1 and S2 show examples of anisotropy measurements for large and small δt values, respectively.

Fig. 4 shows an example of crustal anisotropy measurement at Station 15605 located in the Alxa Block (Fig. 5). Although the P_ms phase can possibly be identified at some BAZ bands before the reverberation removal, the traces are dominated by the strong reverberations with amplitudes that are comparable or greater than that of the P_ms (Fig. 4a), leading to considerable ambiguities in the identification of the P_ms. Due to the strong reverberations which is characterized by the equally spaced alternating positive and negative arrivals with gradually decaying amplitudes (Fig. 4a), it is possible to misidentify one of the positive pulses on the reverberation series as the P_ms phase, and consequently lead to incorrect measurements in Moho depth, crustal Poisson's ratio, and crustal anisotropy. After the application of the reverberation removal technique, the amplitude of the reverberations greatly reduces, and a positive arrival that was largely masked by the reverberations is more clearly observed (Fig. 4b and d). Fig. S3 shows that the two-way traveltimes of the sedimentary layer at the 56 stations applied with the reverberation removal technique (Fig. S3a) have a similar spatial distribution with estimated sediment thickness (Fig. S3b) obtained from a joint inversion of high frequency receiver functions and Rayleigh wave dispersions (Wang et al., 2017b). For example, large two-way traveltimes are found at most stations located in the Yinchuan-Hetao Graben and the Ordos Block, which are consistent with the distribution of thick sediment layer, indicating that the technique can accurately estimate the two-way traveltime of the P_bs. The technique can perform quite well for the reverberations caused by the unconsolidated sedimentary layer, but is not as effective for a consolidated sedimentary layer, so that not all

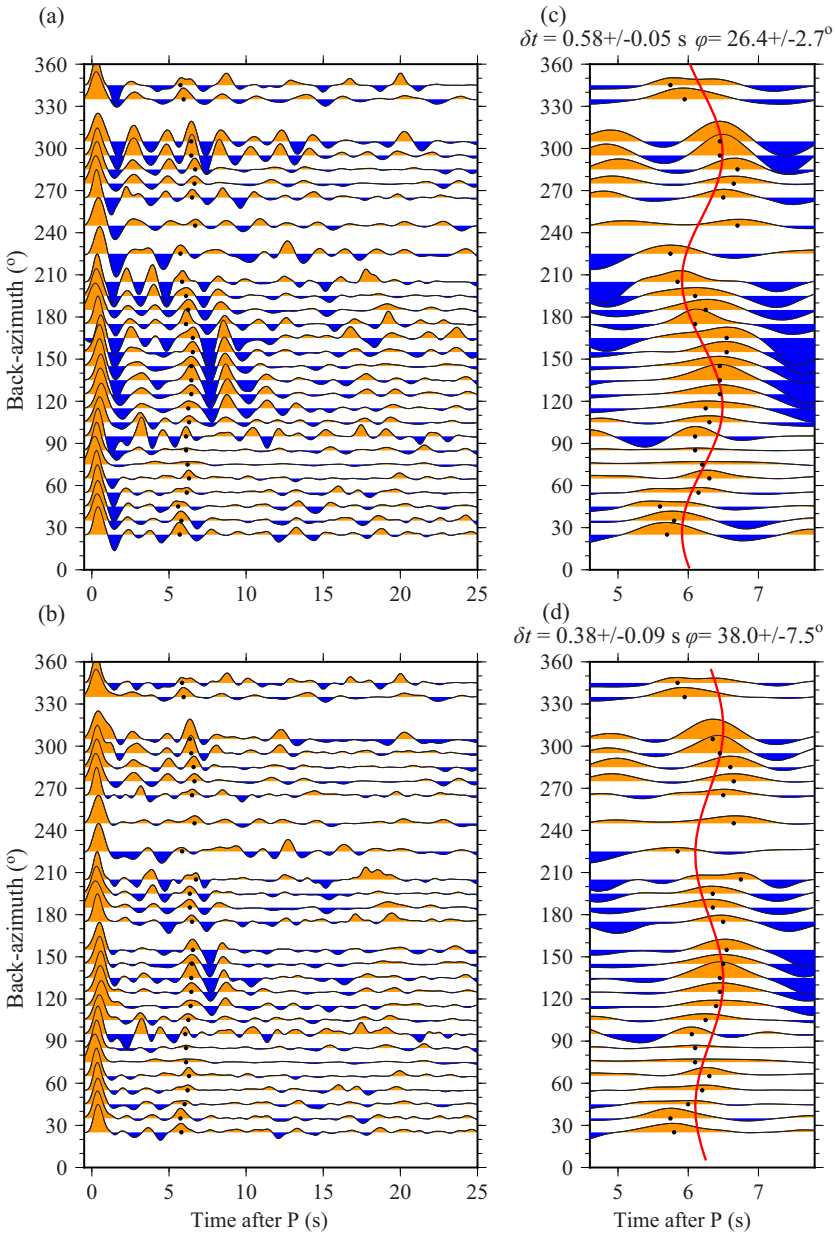

Fig. 4. Measurements of crustal anisotropy at Station 15605 (40.0°N, 103.9°E). (a) BAZ band averaged original radial RFs plotted as a function of the BAZ for the time window of 0–25 s. The black dots on each of the traces indicate the P_ms arrivals. (b) Same as (a) but for RFs after application of the reverberation removal technique. (c) BAZ band averaged original radial RFs for the time window of 4.6–7.8 s. The red curve indicates the theoretical P_ms moveout derived from Eq. (1). (d) Same as (c) but for RFs after application of the reverberation removal technique. (For interpretation of the references to colour in this figure legend, the reader is referred to the web version of this article.)

reverberations can be significantly reduced. We use Station 15717, which is located at the intersection between the Yinchuan-Hetao Graben and the Ordos Block, to demonstrate the effectiveness of the reverberation removal procedure and to explain the difference in the resulting anisotropy parameters between this study and those obtained by Xu et al. (2018). Using the original RFs recorded by Station 15717, Xu et al. (2018) obtained a φ of 27°, which is similar to the φ value that we obtained (28.1 ± 6.4°) before applying the reverberation removal procedure (Fig. S4a and S4c). After applying the reverberation removal technique, the crustal anisotropy parameters for Station 15717 are 160.1 ± 4.1° and 0.38 ± 0.06 s, respectively (Fig. S4b and S4d), which are consistent with those obtained at neighboring stations (Fig. 5).

Most stations observed a single robust P_ms arrival in the expected time window (e.g., Figs. 3a and 4b), which indicates the absence of significant intracrustal layering at the vast majority of the stations and the resultant anisotropy reflects that of the whole crust rather than an anisotropic layer at the base of the crust (Liu et al., 2015; Liu and Park, 2017). In addition, to estimate the influence of a plunging fast axis on the measurements (e.g., Levin and Park, 1998), we generate synthetic RFs using the RAYSUM code (Frederiksen and Bostock, 2000) to demonstrate that the tilted fast axis with a large plunge (30 degree and even as large as 45 degree) does not significantly influence the measured parameters (Fig. S5).

3. Results

Among the 673 stations analyzed, reliable anisotropy parameters were obtained at 246 stations, among which 56 were applied with the reverberation removal technique (Fig. 5 and Table S1). Due to the denser distribution of the seismic stations with reliable measurements, this study has a higher spatial resolution than previous studies using RFs to determine crustal anisotropy (Fig. 1; Shen et al., 2015; Wang et al., 2016). In addition, the application of the reverberation removal procedure to the RFs dramatically increased the number of crustal anisotropy observations within much of the Yinchuan-Hetao Graben and Ordos Block (e.g., Figs. S6 and S7), where only a few measurements were reported by Xu et al. (2018). To the first order, the φ measurements are parallel to the strike of major faults and sutures in the area (Fig. 5).

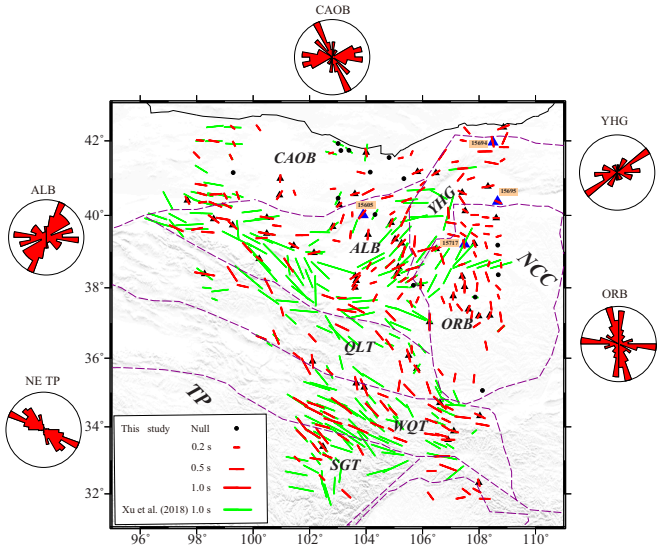

Fig. 5. Crustal anisotropy measurements in the NE Tibetan Plateau and adjacent areas. Red bars are measurements from this study, and green bars are results from Xu et al. (2018). The orientation and length of each bar denote the φ and δt measurements, respectively. The equal-area projection rose diagrams are the distribution of the φ measurements in each of the five tectonic provinces. The black triangles denote the 56 stations with application of the reverberation removal procedure. The black dots are the measurements with magnitude of crustal anisotropy <0.15 s, and we marked them as "Null" measurements (Table S1). The blue triangles indicate the example stations shown in Figs. 4, S4, S6 and S7. Abbreviations are detailed in Fig. 1. (For interpretation of the references to colour in this figure legend, the reader is referred to the web version of this article.)

Additionally, the δt measurements, which have a mean value of 0.36 ± 0.11 s for the study area, have an apparent positive correlation with the intensity of tectonic activity as suggested by the distribution of earthquakes, with larger δt in tectonically more active areas (Fig. 6). For stations with the δt measurements <0.15 s, we marked them as "Null"

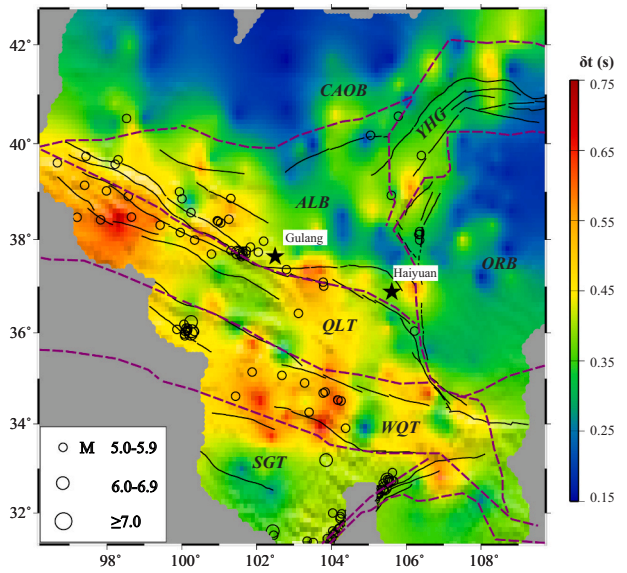

Fig. 6. Spatial distribution of the δt measurements. Circles are large earthquakes occurred over the period of 1980–2020 from the USGS Earthquake Catalog (http://earthquake.usgs.gov/earthquakes/search), and the radius is proportional to event magnitude. The black stars indicate the 1920 M 8.3 Haiyuan and 1927 M 8.0 Gulang earthquakes.

(Table S1 and Fig. S2). These measurements are mainly found in the Central Asia Orogenic Belt and Ordos Block (Fig. 5).

To facilitate discussion, in the following we divide the study area into five tectonic provinces based on major geologic features, and present the results for each of the tectonic provinces and compare our observations with those obtained by previous studies. Table 1 shows the averaged anisotropy parameters and other relevant measurements for each of the tectonic provinces.

3.1. The NE Tibetan Plateau

The NE Tibetan Plateau, including the Qilian, Western Qinling and Songpan-Ganzi terranes, occupies approximately the SW half of the study area. The resulting φ measurements are dominantly NW-SE and E-W, which are mostly consistent with the strike of active faults in the area (Fig. 5). The tectonically active NE Tibetan Plateau has a mean δt of 0.45 ± 0.13 s, which is the largest among all the five regions in the study area (Table 1). Large δt measurements are observed at stations located on the Qilian-Haiyuan Fault and East Kunlun Fault, along which numerous large earthquakes have occurred since 1980 (Fig. 6). The observed measurements are mostly consistent with those obtained by Wang et al. (2016) and Xu et al. (2018), but show some difference from those reported by Shen et al. (2015), who conducted crustal anisotropy investigation in the general area but used a different set of 19 stations. In this area, the crustal φ measurements are generally consistent with the fast orientations from XKS splitting analyses conducted under the assumption of a single layer of anisotropy (Chang et al., 2017), which is generally believed to mostly originate from the mantle (Silver, 1996). The averaged δt (~0.45 s) is about 40% of that obtained from XKS splitting (Table 1), suggesting an important contribution inside the crust to the XKS splitting times (Wang et al., 2016; Zheng et al., 2018; Gao et al., 2019).

Comparing with the previous study conducted by Xu et al. (2018), there are apparently fewer measurements in the Qilian and Songpan-Ganzi terranes from this study. Such a difference is most related to the fact that in this area, Xu et al. (2018) measure crustal anisotropy by combining nearby (in circles with a radius of 0.5°) stations to improve the azimuthal coverage. Given the rapid lateral variation of crustal properties (e.g., Wang et al., 2017b; Zhang et al., 2018) and strong attenuation (e.g., Zhao et al., 2013) in the tectonically complex Tibetan Plateau, we speculate that results from combining stations may not objectively reflect the actual crustal characteristics. For example, in the

Table 1
Averaged GPS directions (Gan et al., 2007; relative to the stable interior of Eurasia) and anisotropy parameters from local S splitting (Liu et al., 2017a; Zhang and Gao, 2017), P_ms moveout and XKS splitting (Ye et al., 2016; Chang et al., 2017; Huang et al., 2017; Gao et al., 2019) for each of the tectonic provinces.

	Northeastern Tibetan plateau	Alxa block	Yinchuan-Hetao graben	Ordos block	Central Asia orogenic belt
GPS (°)	90.9 ± 18.6	74.4 ± 11.8	125.0 ± 14.1	124.0 ± 8.2	67.0 ± 20.2
Local S φ (°)	104.6 ± 39.8	71.2 ± 47.0	25.0 ± 21.2	55.1 ± 33.1	79.6 ± 58.7
Local S normalized δt (ms/km)	5.9 ± 2.61	3.77 ± 1.90	3.04 ± 0.19	2.85 ± 1.45	2.08 ± 1.02
Pms φ (°)	126.7 ± 23.8	80.8 ± 48.7	63.1 ± 37.7	94.2 ± 58.3	102.1 ± 45.1
Pms δt (s)	0.45 ± 0.13	0.37 ± 0.10	0.33 ± 0.12	0.27 ± 0.07	0.28 ± 0.08
XKS φ (°)	110.2 ± 19.4	125.5 ± 13.2	133.8 ± 24.0	115.5 ± 26.5	127.4 ± 17.8
XKS δt (s)	1.12 ± 0.26	1.01 ± 0.27	0.80 ± 0.17	0.73 ± 0.29	0.81 ± 0.15

study of Xu et al. (2018), Station 62397 located on the Qilian Terrane produced anisotropy measurements only when RFs from this station and nearby stations were combined. The number of BAZ bands for Station 62397 is only 8, which does not satisfy the criteria described in Section 2.3. In addition, the δt and φ measurements at Station 51538 located on the Songpan-Ganzi Terrane are 15.5 ± 21.4° and 0.59 ± 0.19 s, respectively, which are quite consistent with the results of Xu et al. (2018), but the combined standard deviation is greater than 0.4, and consequently this station is not included in the analysis because of the large uncertainty in the results. Station 62321 (Fig. S1) is located at the intersection between the Western Qinling Terrane and the Songpan-Ganzi Terrane, where lateral variations of the Moho depth are strong (Wang et al., 2017b; Xu et al., 2018). Compared to Xu et al. (2018), the measurements in this study (113.3 ± 2.1° and 0.75 ± 0.06 s) are more consistent with the results using RFs from single station (127° and 0.8 s) than those from the stations inside the cluster (136° and 1.0 s), suggesting that crustal anisotropy measurements from cluster RFs within a large radius might be biased especially in areas with strong lateral heterogeneities in crustal thickness and velocities.

3.2. Yinchuan-Hetao Graben

In the Yinchuan-Hetao Graben, the φ measurements at most stations are dominantly NE-SW, which are approximately parallel to the margins of the graben. In contrast with the NE Tibetan Plateau, the crustal φ measurements and those from XKS splitting analyses (Chang et al., 2017) in this area are nearly perpendicular to each other. The average δt value from stations located in the Yinchuan-Hetao Graben is 0.33 ± 0.12 s. Because the vast majority of the area is covered by a layer of low-velocity sediments, the application of the reverberation removal technique significantly increased the spatial resolution relative to a previous study using the same data set (Xu et al., 2018), which also reported larger δt measurements at most of the stations than those obtained from the reverberation-removed RFs (Fig. 5).

3.3. Alxa block

The western portion of the Alxa Block shows the same anisotropy pattern as the adjacent Qilian Terrane, with dominantly NW-SE φ and relatively large δt measurements (0.46 ± 0.10 s), whereas the eastern portion of the block shows dominantly NE-SW φ and smaller δt measurements (0.32 ± 0.11 s; Figs. 6 and 7). The observed φ measurements within the block agree well with those from Xu et al. (2018), while the δt measurements from this study are generally lower than those estimated from previous studies (Wang et al., 2016; Xu et al., 2018). Similar to the Yinchuan-Hetao Graben, the low velocity sedimentary layer atop the Alxa Block may cause large uncertainties in the measurements of crustal anisotropy if they are not effectively reduced from the RFs. There is a nearly 90° deviation between the observed φ measurements from this study and those measured from XKS splitting analyses (Chang et al., 2017) in the eastern portion of the block, while the two types of measurements are comparable in the western portion (Figs. 1 and 7).

3.4. Ordos block

A sharp contrast of the observed φ is revealed between the northern and southern portions of the Ordos Block, with nearly E-W φ measurements for the northern part and N-S for the southern part. The orientation of crustal anisotropy for both areas is nearly orthogonal to the fast orientations from XKS splitting analyses (Chang et al., 2017), which show dominantly N-S fast orientations in the northern portion of the Ordos Block and E-W fast orientations in the southern portion (Fig. 1). The observed δt is also shown a N-S difference, with smaller values for the northern and larger values for the southern areas (Fig. 6). The area has the smallest mean δt (0.27 ± 0.07 s) in the entire study area, with smaller δt values in the interior and larger values along the edges

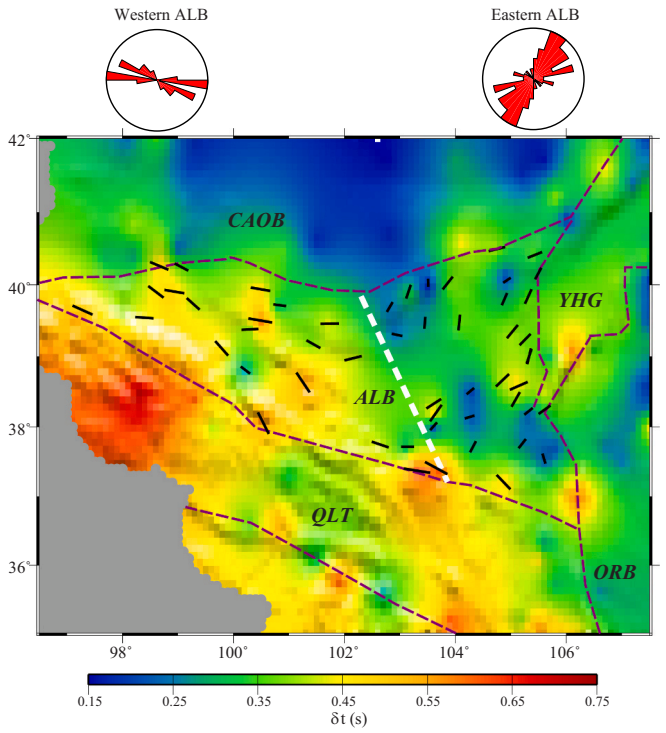

Fig. 7. Crustal anisotropy measurements within the Alxa Block. The background color shows the spatial distribution of the δt measurements. Brown dashed lines mark tectonic boundaries. The white dashed line divides the block into two portions. The two equal-area projection rose diagrams show the distribution of the φ measurements in the western and eastern portions of the Alxa Block, respectively. (For interpretation of the references to colour in this figure legend, the reader is referred to the web version of this article.)

(Fig. 6). Xu et al. (2018) obtained crustal anisotropy measurements at a few stations in this area, with considerable larger δt values, and some are even greater than those from the XKS splitting analysis (Chang et al., 2017). For example, Xu et al. (2018) obtained a large δt of 1.3 s (while the splitting time obtained by Chang et al., 2017 using the XKS phase is merely 0.56 s) at Station 15717 (Fig. 5 and S4). After applying the reverberation removal technique, the value of δt from this study is 0.38 s, which is comparable to that observed at neighboring stations.

3.5. Central Asia orogenic belt

The observed φ measurements at stations located near the southern edge of the Central Asian Orogenic Belt are mostly consistent with the trend of the orogenic belt, and those at stations within the orogenic belt are dominantly E-W with a few N-S or NW-SE measurements. This area has a small mean δt (0.28 ± 0.08 s) in the study area. While some differences exist at some stations, the measurements from this study are generally consistent with those obtained by Xu et al. (2018), although the former has about twice as many measurements as the latter in this area (Fig. 5).

4. Discussion

4.1. Fracture-induced crustal anisotropy beneath the NE Tibetan Plateau

The φ measurements in the tectonically active NE Tibetan Plateau are dominantly fault-parallel (NW-SE), in the vicinity of the strike-slip faults (Fig. 5), in which numerous large earthquakes have been recorded (Fig. 6). This pattern of crustal anisotropy is consistent with the GPS-based conclusion that shear strain is strongly localized along the Qilian-Haiyuan and East Kunlun Faults (Fig. 8; Li et al., 2018). Chang et al.

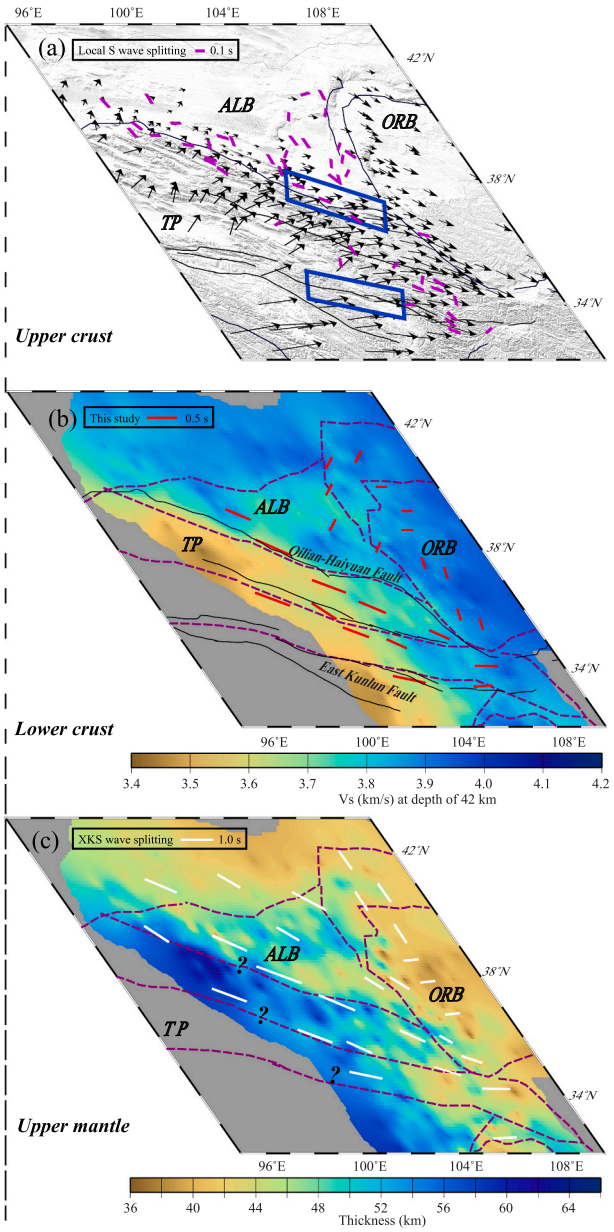

Fig. 8. (a) Upper crustal deformation pattern in the NE Tibetan Plateau and adjacent areas. The black arrows show the GPS velocities relative to the stable Eurasian Plate (Gan et al., 2007). The blue boxes indicate the region where the shear strain rates are anomalously high (Li et al., 2018). The purple bars represent local S splitting measurements (Liu et al., 2017a; Zhang and Gao, 2017). (b) Bulk crustal anisotropy in the NE Tibetan Plateau and adjacent areas constructed based on our measurements. The red bars are representative measurements showing the major characteristics of the crustal anisotropy pattern. The background color represents V_S at depth of 42 km (Wang et al., 2017b). The black lines in the crust outline the deep active faults. (c) Upper mantle deformation pattern in the NE Tibetan Plateau and adjacent areas. The white bars are representative XKS splitting measurements showing the major characteristics of the upper mantle anisotropy pattern (Chang et al., 2017). The background color represents the crustal thickness (Wang et al., 2017b). The question marks indicate possible lithosphere-scale faults. (For interpretation of the references to colour in this figure legend, the reader is referred to the web version of this article.)

(2017) present a dominant NW-SE predicted fast axis measurement in the NE Tibetan Plateau from the surface deformation field based on the GPS observations and fault slip rates. The consistency between the structural crustal features, the predicted fast axis inferred from the surface deformation field, and the observed crustal anisotropy reveals that the left-lateral strike slip faults in the NE Tibetan Plateau have a significant influence on the whole crust. The fault-parallel orientations may thus represent fabric that evolved as a response to present-day ongoing deformation. Alternatively, the observed crustal anisotropy may reflect pre-existing fabric produced by previous tectonic episodes, along which the faults developed. This hypothesis is consistent with the observation that unlike observations made in some other areas such as the North China Craton (e.g., Zheng et al., 2019), a clear increase in the δt values in major fault zones is not observed in most of the study area (Fig. 6). While in reality both active faults and pre-existing fabric may contribute to the observed crustal anisotropy, additional investigations are needed in order to pinpoint the contributions from each of the sources.

The distribution of regional earthquakes in the NE Tibetan Plateau suggests that most events concentrated in the depth range of 0–15 km (Wei et al., 2010), indicating a significant brittle deformation in the upper crust. Direct S-wave splitting measurements (Liu et al., 2017a; Zhang and Gao, 2017) from local earthquakes with focal depths of 5–15 km in the upper crust obtained an average normalized δt of 5.9 ± 2.61 ms/km in the NE Tibetan Plateau, which is equivalent to a δt of 0.15 s for a 25 km thick upper crust. The remaining crustal δt, which amounts 0.45 s on average in the NE Tibetan Plateau, is primarily attributable to the middle-to-lower crust. In addition, the distribution of large earthquakes is closely related to the active faults (Fig. 6), and a seismic reflection study (Wang et al., 2011) across the Kunlun Fault suggests a duplex crust with the upper and lower decollements and a thrust fault system cutting across the Moho. A receiver function study using data from a passive seismic array in the northeastern Tibetan Plateau also indicated that some major faults such as the East Kunlun Fault and the Qinling Fault cut the Moho (Shen et al., 2014). The observed crustal anisotropy suggests pervasive existence of fault-parallel fabrics in both the upper and middle-lower crust beneath the NE Tibetan Plateau.

4.2. *Crustal flow beneath the NE Tibetan Plateau?*

Shen et al. (2015) conduct crustal anisotropy measurements using data from 19 stations in the NE Tibetan Plateau and reveal NE-SW trending crustal anisotropy at some of the stations, which is attributed to lower crustal flow beneath the NE margin of the Tibetan Plateau (Clark and Royden, 2000). Additionally, several studies (e.g., Jiang et al., 2014) show a prominent low velocity zone beneath a large part of the NE Tibetan Plateau and western Alxa Block, which is interpreted as the manifestation of a middle or/and lower crustal channel flow system.

In contrast, a more recent study (Wang et al., 2017b) with an improved spatial resolution suggests the absence of widespread low velocity anomalies in the lower crust. The lack of a large scale and continuous low velocity zone in the lower crust suggest that the lower crust has a high viscosity that is not in favor of the crustal ductile flow model (Bao et al., 2013; Wang et al., 2017b). The crustal flow model does not necessarily mean lower crustal flow, and it could be middle crustal channel flow within the thick-crust Tibetan Plateau (e.g., Clark and Royden, 2000), but the low velocity zones in the middle crust of the NE Tibetan Plateau are mostly narrow and isolated features which are inconsistent with the presence of plastic flow in the middle crust (Fig. 9 in Wang et al., 2017b). More importantly, crustal Vp/Vs values in the NE Tibetan Plateau and western Alxa Block are normal to lower than normal (Wang et al., 2017a). Laboratory experiments suggest that crustal Vp/Vs ratio is related to rock types and is useful in constraining the component of the crust. Additionally, partial melting leads to elevated Vp/Vs values due to the stronger reduction of Vs. Therefore, the observed normal to lower than normal Vp/Vs values indicate that the absence of pervasive

partial melting in the middle and lower crust of the NE Tibetan Plateau and western Alxa Block, further implying that the channel flow in the middle-to-lower crust is unlikely to exist (Wang et al., 2017a). Additionally, the ambient noise tomography using a similar set of data as this study reveals a weak and negative radial anisotropy ($V_{SH} < V_{SV}$) beneath the NE Tibetan Plateau (Yang et al., 2019), which is consistent with the pattern of radial anisotropy obtained by surface waves of natural earthquakes (Chen et al., 2009; Xie et al., 2013). The pattern is supportive of the mechanism of lateral crustal shortening and vertical thickening but not the existence of middle-to-lower crustal flow.

These results from previous studies of crustal structure, when combined with the significant discrepancies between the crustal anisotropy measurements from this study and proposed flow direction, are incompatible with the crustal ductile flow model. The dominantly NW-SE fast orientations pervasively observed in NE Tibetan Plateau are inconsistent with the proposed NE orientation of the lower crustal flow (Shen et al., 2015). This is in sharp contrast with the SE Tibetan Plateau, where crustal radial anisotropy (Yang et al., 2019) and azimuthal anisotropy (Kong et al., 2016; Zheng et al., 2018) measurements suggest that middle-to-lower crustal flow might be the dominant mechanism responsible for crustal thickening.

4.3. Possible crustal modification beneath the Alxa block

Whether or not the Alxa Block is a part of the stable North China Craton remains controversial (Dan et al., 2016; Yu and Chen, 2016; Guo et al., 2017; Shen et al., 2017). Geological evidence from Paleozoic granitoids and geochronology argues that the Alxa Block is not likely a component of the North China Craton (Dan et al., 2016). Shen et al. (2017) show strong lithospheric deformation and thickening beneath the NE Tibetan Plateau but insignificant deformation in the Alxa Block, suggesting that the lithospheric structure of the whole Alxa Block is not affected by the processes forming the Tibetan Plateau.

The crustal anisotropy features revealed by this study (Fig. 7) show that the observed measurements in the western portion of the Alxa Block are dominantly NW-SE with an average δt value of 0.46 ± 0.10 s, which are comparable to those observed in the neighboring Qilian Terrane (average δt of 0.51 ± 0.12 s) of the NE Tibetan Plateau. In contrast, the fast orientation in the eastern portion of the block is approximately NE-SW with an average δt of 0.32 ± 0.11 s, suggesting different crustal deformation direction and strength between the western and eastern halves of the Alxa Block. Additionally, clear differences in lithospheric structure between the western and eastern portions of the Alxa Block are revealed by previous studies (e.g., An and Shi, 2006; Guo et al., 2017; Wang et al., 2017a, 2017b). The western portion of the Alxa Block is characterized by a thick crust (~ 50 km, Wang et al., 2017b) and a thin lithosphere (An and Shi, 2006), with low crustal Poisson's ratios (Wang et al., 2017a) and low shear wave velocity in the crust and lithospheric mantle (Guo et al., 2017), especially along the western edges of the Alxa Block where the lithospheric structures are quite consistent with the neighboring Qilian Terrane (Fig. 8). In contrast, the eastern portion exhibits a thinner crust (~ 45 km) and a thicker lithosphere, with moderate-to-high crustal Poisson's ratios and higher lithospheric velocity, which are comparable to the stable North China Craton (Zhang et al., 2018). These sharp contrasts in lateral heterogeneities within the Alxa Block, together with the significant contrasts in the φ and δt measurements between the western and eastern portions of the block revealed by this study, suggest that the crustal structure in the western portion of the Alxa Block may be modified by the far field stress originated from the collision between the Indian and Eurasian plates, whereas the eastern portion of the Alxa Block was less influenced and may preserve its old cratonic root.

5. Conclusions

Using a seismic data set recorded by the ChinArray-Himalaya II seismic array that covered the NE Tibetan Plateau and adjacent areas, this study quantified crustal anisotropy based on the azimuthal moveout of P-to-S conversions from the Moho. The application of the reverberation removal technique to the RFs resulted in better constrained estimations of crustal anisotropy than studies using the original RFs. The main findings of this study include: (1) Anisotropy observations beneath the tectonically active plateau are closely related to the strike-slip faults rather than channel flow in the middle-to-lower crust. (2) Spatial distributions of the measured crustal anisotropy provide additional evidence for crustal modification beneath the western portion of the Alxa Block, probably induced by the far field effect of the Indo-Eurasian collision. (3) The eastern portion of the Alxa Block is less influenced by the collision, probably due to the resistance of the Ordos Block which restricts the lateral growth of the Tibetan Plateau.

Declaration of Competing Interest

The authors declare that they have no known competing financial interests or personal relationships that could have appeared to influence the work reported in this paper.

Acknowledgment

The waveform data were provided by the Data Management Center of China National Seismic Network at Institute of Geophysics, China Earthquake Administration. We thank X.C. Wang for calculating the original RFs used in this study. The receiver functions used in the study can be freely downloaded from https://zenodo.org/record/4692361. This work is supported by the National Key Research and Development Program of China (grant 2017FYC1500200 to Z.D.), and the National Natural Science Foundation of China (grants 42004078 to T.Z., and 41874051 to X.F.), the State Key Laboratory of Marine Geology, Tongji University (grant MGK202012 to T.Z.), and the United States National Science Foundation (grants 1321656 and 1830644 to K.L. and S.G., and grant 1919789 to S.G.).

Appendix A. Supplementary data

Supplementary data to this article can be found online at https://doi.org/10.1016/j.tecto.2021.229014.

References

An, M., Shi, Y., 2006. Lithospheric thickness of the Chinese continent. Phys. Earth Planet. Inter. 159, 257–266. https://doi.org/10.1016/j.pepi.2006.08.002.

Bao, X., Song, X., Xu, M., Wang, L., Sun, X., Mi, N., Yu, D., Li, H., 2013. Crust and upper mantle structure of the North China Craton and the NE Tibetan Plateau and its tectonic implications. Earth Planet. Sci. Lett. 369–370, 129–137. https://doi.org/10.1016/j.epsl.2013.03.015.

Chang, L., Ding, Z., Wang, C., Flesch, L.M., 2017. Vertical coherence of deformation in lithosphere in the NE margin of the Tibetan plateau using GPS and shear-wave splitting data. Tectonophysics 699, 93–101. https://doi.org/10.1016/j.tecto.2017.01.025.

Chen, Y., Badal, J., Zhang, Z., 2009. Radial anisotropy in the crust and upper mantle beneath the Qinghai-Tibet Plateau and surrounding regions. J. Asian Earth Sci. 36 (4–5), 289–302. https://doi.org/10.1016/j.jseaes.2009.06.011.

Clark, M.K., Royden, L.H., 2000. Topographic ooze: building the eastern margin of Tibet by lower crustal flow. Geology 28, 703–706.

Crampin, S., 1978. Seismic-wave propagation through a cracked solid: polarization as a possible dilatancy diagnostic. Geophys. J. Int. 53 (3), 467–496. https://doi.org/10.1111/j.1365-246X.1978.tb03754.x.

Dan, W., Li, X., Wang, Q., Wang, X., Wyman, D.A., Liu, Y., 2016. Phanerozoic amalgamation of the Alxa Block and North China Craton: evidence from Paleozoic granitoids, U-Pb geochronology and Sr-Nd-Pb-Hf-O isotope geochemistry. Gondwana Res. 32, 105–121. https://doi.org/10.1016/j.gr.2015.02.011.

Efron, B., Tibshirani, R., 1986. Bootstrap methods for standard errors, confidence intervals, and other measures of statistical accuracy. Stat. Sci. 1 (1), 54–75. https://doi.org/10.1214/ss/1177013815.

England, P., Houseman, G., 1986. Finite strain calculations of continental deformation: comparison with the India-Asia collision zone. J. Geophys. Res. Solid Earth 91 (B3), 3664–3676. https://doi.org/10.1029/JB091iB03p03664.

Frederiksen, A.W., Bostock, M.G., 2000. Modelling teleseismic waves in dipping anisotropic structures. Geophys. J. Int. 142 (2), 401–412. https://doi.org/10.1046/j.1365-246X.2000.00090.x.
Gan, W., Zhang, P., Shen, Z., Niu, Z., Wang, M., Wan, Y., Zhou, D., Cheng, J., 2007. Present-day crustal motion within the Tibetan Plateau inferred from GPS measurements. J. Geophys. Res. Solid Earth 112, B08416. https://doi.org/10.1029/2005JB004120.
Gao, S.S., Liu, K.H., 2014. Mantle transition zone discontinuities beneath the contiguous United States. J. Geophys. Res. Solid Earth 119, 6452–6468. https://doi.org/10.1002/2014JB011253.
Gao, Y., Chen, L., Wang, X., Ai, Y., 2019. Complex lithospheric deformation in eastern and northeastern Tibet from shear-wave splitting observations and its geodynamic implications. J. Geophys. Res. Solid Earth 124 (10), 10331–10346. https://doi.org/10.1029/2018JB017081.
Guo, H., Ding, Z., Xu, X., 2017. Upper mantle structure beneath the northern South-North Seismic Zone from teleseimic traveltime data. Chin. J. Geophys. (in Chinese) 60 (1), 86–97. https://doi.org/10.6038/cjg20170108.
Hacker, B.R., Ritzwoller, M.H., Xie, J., 2014. Partially melted, mica-bearing crust in Central Tibet. Tectonics 33, 1408–1424.
Huang, Z., Wang, P., Zhao, D., Wang, L., Xu, M., 2014. Three-dimensional P wave azimuthal anisotropy in the lithosphere beneath China. J. Geophys. Res. Solid Earth 119, 5686–5712. https://doi.org/10.1002/2014JB010963.
Huang, Z., Frederik, T., Xu, M., Wang, L., Ding, Z., Mi, N., Yu, D., Li, H., 2017. Insight into NE Tibetan Plateau expansion from crustal and upper mantle anisotropy revealed by shear-wave splitting. Earth Planet. Sci. Lett. 478, 66–75. https://doi.org/10.1016/j.epsl.2017.08.030.
Jiang, C., Yang, Y., Zheng, Y., 2014. Penetration of mid-crustal low velocity zone across the Kunlun fault in the NE Tibetan Plateau revealed by ambient noise tomography. Earth Planet. Sci. Lett. 406 (3), 369–382. https://doi.org/10.1016/j.epsl.2014.08.040.
Kong, F., Wu, J., Liu, K.H., Gao, S.S., 2016. Crustal anisotropy and ductile flow beneath the eastern Tibetan Plateau and adjacent areas. Earth Planet. Sci. Lett. 442, 72–79. https://doi.org/10.1016/j.epsl.2016.03.003.
Levin, V., Park, J., 1998. P-SH conversions in layered media with hexagonally symmetric anisotropy: a cook book. Pure Appl. Geophys. 151 (2–4), 669–697. https://doi.org/10.1007/s000240050136.
Li, Y., Liu, M., Wang, Q., Cui, D., 2018. Present-day crustal deformation and strain transfer in northeastern Tibetan Plateau. Earth Planet. Sci. Lett. 35, 179–189. https://doi.org/10.1016/j.epsl.2018.01.024.
Ligorria, J.P., Ammon, C.J., 1999. Iterative deconvolution and receiver-function estimation. Bull. Seismol. Soc. Am. 89 (5), 1395–1400.
Liu, H., Niu, F., 2012. Estimating crustal seismic anisotropy with a joint analysis of radial and transverse receiver function data. Geophys. J. Int. 188 (1), 144–164. https://doi.org/10.1111/j.1365-246X.2011.05249.x.
Liu, Z., Park, J., 2017. Seismic receiver function interpretation: Ps splitting or anisotropic underplating? Geophys. J. Int. 208, 1332–1341. https://doi.org/10.1093/gji/ggw455.
Liu, K.H., Gao, S.S., Silver, P.G., Zhang, Y.K., 2003. Mantle layering across central South America. J. Geophys. Res. Solid Earth 108, 2510. https://doi.org/10.1029/2002JB002208.
Liu, Z., Park, J., Rye, D.M., 2015. Crustal anisotropy in northeastern Tibetan Plateau inferred from receiver functions: rock textures caused by metamorphic fluids and lower-crust flow? Tectonophysics 661, 66–80. https://doi.org/10.1016/j.tecto.2015.08.006.
Liu, G., Gao, Y., Shi, Y., 2017a. Shear wave splitting in Qinling Orogen and its both sides. Chin. J. Geophys. (in Chinese) 60 (6), 2326–2337. https://doi.org/10.6038/cjg20170624.
Liu, L., Gao, S.S., Liu, K.H., Mickus, K., 2017b. Receiver function and gravity constraints on crustal structure and vertical movements of the Upper Mississippi Embayment and Ozark Uplift. J. Geophys. Res. Solid Earth 122, 4572–4583. https://doi.org/10.1002/2017JB014201.
Molnar, P., Tapponnier, P., 1975. Cenozoic tectonics of Asia: effects of a continental collision. Science 189 (4201), 419–426. https://doi.org/10.1126/science.189.4201.419.
Nagaya, M., Oda, H., Akazawa, H., Ishise, M., 2008. Receiver functions of seismic waves in layered anisotropic media: application to the estimate of seismic anisotropy. Bull. Seismol. Soc. Am. 98 (6), 2990–3006. https://doi.org/10.1785/0120080130.
Rasolofosaon, P.N.J., Rabbel, W., Siegesmund, S., Vollbrecht, A., 2000. Characterization of crack distribution: fabric analysis versus ultrasonic inversion. Geophys. J. Int. 141 (2), 413–424. https://doi.org/10.1046/j.1365-246x.2000.00093.x.
Rumpker, G., Kaviani, A., Latifi, K., 2014. Ps-splitting analysis for multilayered anisotropic media by azimuthal stacking and layer stripping. Geophys. J. Int. 199 (1), 146–163. https://doi.org/10.1093/gji/ggu154.
Shen, X., Yuan, X., Zhang, Y., Mei, X., Guo, X., Liu, X., Qin, M., Wei, C., Li, C., 2014. Receiver function structures beneath the deep large faults in the northeastern margin of the Tibetan Plateau. Tectonophysics 610, 63–73. https://doi.org/10.1016/j.tecto.2013.10.011.
Shen, X., Yuan, X., Ren, J., 2015. Anisotropic low-velocity lower crust beneath the northeastern margin of Tibetan Plateau: evidence for crustal channel flow. Geochem. Geophys. Geosyst. 16, 4223–4236.
Shen, X., Liu, M., Gao, Y., Wang, W., Shi, Y., An, M., Zhang, Y., Liu, X., 2017. Lithospheric structure across the northeastern margin of the Tibetan Plateau: implications for the plateau's lateral growth. Earth Planet. Sci. Lett. 459, 80–92. https://doi.org/10.1016/j.epsl.2016.11.027.
Silver, P.G., 1996. Seismic anisotropy beneath the continents: probing the depths of geology. Annu. Rev. Earth Planet. Sci. 24, 385–432. https://doi.org/10.1146/annurev.earth.24.1.385.
Tapponnier, P., Zhiqin, X., Roger, F., Meyer, B., Arnaud, N., Wittlinger, G., Jingsui, Y., 2001. Oblique stepwise rise and growth of the Tibet Plateau. Science 294 (5547), 1671–1677. https://doi.org/10.1126/science.105978.
Tatham, D.J., Lloyd, G.E., Butler, R.W.H., Casey, M., 2008. Amphibole and lower crustal seismic properties. Earth Planet. Sci. Lett. 267 (1–2), 118–128. https://doi.org/10.1016/j.epsl.2007.11.042.
Wang, C.S., Gao, R., Yin, A., Wang, H.Y., Zhang, Y.X., Guo, T.L., Li, Q.S., Li, Y.L., 2011. A mid-crustal strain-transfer model for continental deformation: a new perspective from high-resolution deep seismic-reflection profiling across NE Tibet. Earth Planet. Sci. Lett. 306, 279–288. https://doi.org/10.1016/j.epsl.2011.04.010.
Wang, Q., Niu, F., Gao, Y., Chen, Y., 2016. Crustal structure and deformation beneath the NE margin of the Tibetan Plateau constrained by teleseismic receiver function data. Geophys. J. Int. 204 (1), 167–179.
Wang, W., Wu, J., Fang, L., Lai, G., Cai, Y., 2017a. Sedimentary and crustal thicknesses and Poisson's ratios for the NE Tibetan Plateau and its adjacent regions based on dense seismic arrays. Earth Planet. Sci. Lett. 462, 76–85. https://doi.org/10.1016/j.epsl.2016.12.040.
Wang, X., Li, Y., Ding, Z., Zhu, L., Wang, C., Bao, X., Wu, Y., 2017b. Three-dimensional lithospheric S wave velocity model of the NE Tibetan Plateau and western North China Craton. J. Geophys. Res. Solid Earth 122, 6703–6720. https://doi.org/10.1002/2017JB014203.
Wei, S.Q., Chen, J.Y., Sandvol, E., et al., 2010. Regional earthquakes in northern Tibetan Plateau: implications for lithospheric strength in Tibet. Geophys. Res. Lett. 37 https://doi.org/10.1029/2010GL044800. L19307.
Xie, J., Ritzwoller, M.H., Shen, W., et al., 2013. Crustal radial anisotropy across Eastern Tibet and the Western Yangtze Craton. J. Geophys. Res. Solid Earth 118, 1–27. https://doi.org/10.1002/jgrb.50296.
Xie, J., Ritzwoller, M.H., Shen, W., Wang, W., 2017. Crustal anisotropy across eastern Tibet and surroundings modeled as a depth-dependent tilted hexagonally symmetric medium. Geophys. J. Int. 209, 466–491. https://doi.org/10.1093/gji/ggx004.
Xu, X., Niu, F., Ding, Z., Chen, Q., 2018. Complicated crustal deformation beneath the NE margin of the Tibetan Plateau and its adjacent areas revealed by multi-station receiver-function gathering. Earth Planet. Sci. Lett. 497, 204–216. https://doi.org/10.1016/j.epsl.2018.06.010.
Yang, Z., Chen, Y., Zhang, X., Song, X., 2019. S-wave velocity structure and radial anisotropy in eastern and north-eastern margins of Tibetan Plateau. Chin. J. Geophys. (in Chinese) 62 (12), 4554–4570. https://doi.org/10.6038/cjg2019N0149.
Ye, Z., Li, Q., Gao, R., Zhang, H., Shen, X., Liu, X., Gong, C., 2016. Anisotropic regime across northeastern Tibet and its geodynamic implications. Tectonophysics 671, 1–8. https://doi.org/10.1016/j.tecto.2016.01.011.
Yin, A., Harrison, T.M., 2000. Geologic evolution of the Himalayan-Tibetan orogen. Annu. Rev. Earth Planet. Sci. 28, 211–280. https://doi.org/10.1146/annurev.earth.28.1.211.
Yu, Y., Chen, Y.J., 2016. Seismic anisotropy beneath the southern Ordos block and the Qinling-Dabie orogen, China: Eastward Tibetan asthenospheric flow around the southern Ordos. Earth Planet. Sci. Lett. 455, 1–6. https://doi.org/10.1016/j.epsl.2016.08.026.
Yu, Y.Q., Song, J.G., Liu, K.H., Gao, S.S., 2015. Determining crustal structure beneath seismic stations overlying a low-velocity sedimentary layer using receiver functions. J. Geophys. Res. Solid Earth 120, 3208–3218. https://doi.org/10.1002/2014JB011610.
Zelt, B.C., Ellis, R.M., 1999. Receiver-function studies in the Trans-Hudson orogen, Saskatchewan. Can. J. Earth Sci. 36, 585–603. https://doi.org/10.1139/cjes-36-4-585.
Zhang, Y., Gao, Y., 2017. The characteristics of crustal shear wave splitting in North South seismic zone revealed by near field recordings of two observation periods of Chin Array. Chin. J. Geophys. (in Chinese) 60 (6), 2181–2199. https://doi.org/10.6038/cjg20170613.
Zhang, S., Karato, S., 1995. Lattice preferred orientation of olivine aggregates deformed in simple shear. Nature 375, 774–777.
Zhang, F., Wu, Q., Li, Y., Zhang, R., Sun, L., Pan, J., Ding, Z., 2018. Seismic tomography of eastern Tibet: implications for the Tibetan Plateau growth. Tectonics 37, 2833–2847. https://doi.org/10.1029/2018TC004977.
Zhao, L., Xie, X., He, J., Tian, X., Yao, Z., 2013. Crustal flow pattern beneath the Tibetan Plateau constrained by regional Lg-wave Q tomography. Earth Planet. Sci. Lett. 383, 113–122. https://doi.org/10.1016/j.epsl.2013.09.038.
Zheng, T., Ding, Z., Ning, J., Chang, L., Wang, X., Kong, F., Liu, K.H., Gao, S.S., 2018. Crustal azimuthal anisotropy beneath the southeastern Tibetan Plateau and its geodynamic implications. J. Geophys. Res. Solid Earth 123 (11), 9733–9749. https://doi.org/10.1029/2018JB015995.
Zheng, T., Ding, Z., Ning, J., Liu, K.H., Gao, S.S., Chang, L., Kong, F., Fan, X., 2019. Crustal azimuthal anisotropy beneath the central North China Craton revealed by receiver functions. Geochem. Geophys. Geosyst. 20, 2235–2251. https://doi.org/10.1029/2019GC008181.
Zhu, T., Ma, X., 2021. Uppermantle shear-wave splitting measurements in Mainland China: a review. Earth-Sci. Rev. 212, 103437. https://doi.org/10.1016/j.earscirev.2020.103437.